https://dx.doi.org/10.1016/j.istruc.2024.108104

A Multifaceted Study of Embedded Seismic Metamaterials: Bridging Unit Cells, Bandgaps, and Multi-Domain Characteristics

Hongshan Pan

Ph.D. Student

Email: hong-shan.pan@connect.polyu.hk

Department of Civil and Environmental Engineering

The Hong Kong Polytechnic University

Kai Zhou†, Ph.D. (Corresponding author)

Assistant Professor

Email: cee-kai.zhou@polyu.edu.hk

Department of Civil and Environmental Engineering

Research Institute for Sustainable Urban Development (RISUD)

The Hong Kong Polytechnic University

Submitted to: Structures (Revised)

A Multifaceted Study of Embedded Seismic Metamaterials: Bridging Unit Cells, Bandgaps, and Multi-Domain Characteristics

Hongshan Pan and Kai Zhou†

Department of Civil and Environmental Engineering, The Hong Kong Polytechnic University, Hong Kong, China

Abstract: Seismic metamaterials (SMs) are an emerging technology for seismic mitigation. Existing studies have primarily focused on optimizing the configuration of SM unit cells to broaden the bandgap. However, the bandgap, as a highly idealized indicator, is built upon the assumption of a fully periodic arrangement of unit cells and cannot quantify the actual seismic attenuation of SMs under many practical circumstances. System-level approaches, such as time-domain and frequency-domain analyses, offer more pragmatic evaluations of the SM performance. Nevertheless, the complex interrelationships among these measures pose significant challenges for effective assessment. Therefore, this research aims to elucidate the intrinsic correlations among unit cell configuration, bandgap, and multi-domain characteristics, including frequency transmission and time transient behavior. A fully embedded SM is developed for in-depth investigations. High-fidelity finite element models are developed to characterize the bandgaps and multi-domain responses of the SM. Time transient analysis incorporating actual earthquake-induced ground motion data indicates the SM's ability to attenuate real seismic waves. The attenuation spectrum extracted from the time transient analysis closely corresponds with that observed in frequency transmissions, regardless of SM operational conditions. Additionally, while bandgap analysis is efficient, relying solely on the bandgap is insufficient for quantifying SM wave attenuation performance. On the other hand, a combination of multi-domain analyses provides a more comprehensive metric for performance assessment, thereby contributing to future SM design.

Keywords: Seismic metamaterial; unit cell; bandgap; transmission; time transient analysis; seismic wave propagation.

1. Introduction

1.1. Earthquake mitigation and seismic metamaterials

Earthquakes are natural disasters caused by tectonic movements within the Earth's interior, typically occurring in fault zones or plate boundaries. When the stress between plates accumulates to a certain level, it triggers an earthquake. The energy released by earthquakes propagates in the form of low-frequency seismic waves (below 20Hz) [1], leading to the collapse of buildings and other infrastructure. Traditional seismic protecting measures, such as dampers and seismic bearings [2-7], often come with unacceptable residual displacements and limited seismic energy absorption, thus necessitating new methods to protect infrastructure from earthquake damage.

Seismic metamaterials (SMs), as a revolutionary technology, present a novel approach to controlling ground-borne waves, including seismic waves, thereby capable of mitigating seismic disasters for infrastructures [8-14] and attenuating the impact and vibration induced by explosive blast [15]. SMs are normally comprised of periodically arranged unit structures, referred to as unit cells, and exhibit a performance-related characteristic, known as bandgaps, which denote specific frequency ranges where the propagation of seismic waves is blocked [16]. Specifically, due to their capacity to impede seismic waves using relatively compact SM dimensions, SMs based on local resonance show tremendous potential for practical applications [17-20]. This type of SMs is composed of soil substrates and resonators, with the latter being the most important components, generating bandgaps through their local resonance effects and absorbing seismic energy [21].

1.2. Related works

Currently, local resonance-based SMs have been extensively investigated. Featuring local resonators erected on the soil surface, a typical type of SMs, referred to as above-soil SMs, normally constructed from steel or concrete, represent the prevailing design due to their low design costs and desired environmental sustainability [22]. Geometric design, particularly the cross-sectional design of the columns, is essential for achieving broad bandgaps [23]. In addition to commonly used shapes, such as rectangular, cylindrical, and built-up cross-sections [24-27], research has also explored the potential of more intricate geometric shapes, such as fractal-based column section designs or nested structures, to enhance seismic wave shielding capabilities [28-30].

Despite the cost advantages in design, the practical application of above-soil SMs faces challenges. Firstly, due to their above-ground nature, they occupy roadways or building sites, leading to land scarcity, especially in urban areas. Secondly, above-soil SMs can obstruct views, posing a potential threat to pedestrian and traffic safety. Additionally, current research primarily focuses on the design of the cross sections of local resonators, while neglecting the design of connections between overground resonators and the soil surface. Embedded SMs, with local resonators fully embedded in the soil [31], show promise to address these issues. Although more suitable for engineering practice, the local resonance of the embedded resonators is constrained by the surrounding soil, limiting the resonance effects. To mitigate the constraints of the embedded resonators exerted by the soil, flexible materials, such as rubber, are adopted to separate the soil and resonators. For instance, an embedded local resonator composed of concrete spheres enveloped in rubber layers was designed by Chen et al. [32], demonstrating its low-frequency wave attenuation performance. Daradkeh et al. [33] proposed large-scale engineered meta-barriers where the embedded. unit cells were composed of rubber shells and cubic steel cores and analyzed the influence of unit cell graded configurations on the wave attenuation. Similarly, Wu et al. [34] proposed a local resonator by wrapping a rubber pad around an embedded concrete block, demonstrating a bandgap ranging from 11.69 to 12.78 Hz. Utilizing *H*-shaped steel blocks encased with rubber, an embedded SM was designed by Xu et al. [35], with a total bandgap width of 7.95 Hz. In the research conducted by Daradkeh et al. [36], embedded SM design was proposed. The local resonators were composed of rubber covers and different core materials, including concrete, steel, and carbon fiber-reinforced polymer. The influence of different core materials and unit cell graded layout patterns on the wave blocking performance was studied. Daradkeh [37] also carried out a systematic investigation, where different multi-layered embedded unit cells with multiple graded arrangements were developed, and the seismic wave blocking capabilities were examined using real-world seismic accelerations.

Despite the certain level of success in unit cell design to achieve the broad bandgap as introduced earlier, it is worth mentioning that the bandgap, based on the unit cell configuration, is an ideal indicator and may not provide a rigorous performance assessment of the entire SM. This is due to several reasons: 1). The bandgap is not experimentally measurable in real operational conditions; 2). Theoretically, the bandgap can accurately estimate the performance of the entire SM only when the SM is comprised of *an infinite number of identical unit cells*, which contradicts practical SM deployments; 3) Seismic waves, in the form of surface and bulk waves, exhibit complex behavior when propagating within the SM, influenced by many realistic factors, such as wave reflection effect. In order to quantify the seismic wave attenuation performance with a limited number of unit cells arranged in the direction of wave propagation, the frequency domain analysis (FDA) [38-40] is widely adopted. By applying frequency-sweeping harmonic excitation to SMs and calculating the transmission indicator, the attenuation effect of SMs on seismic waves at different frequencies can be evaluated. In addition, given that seismic waves in reality are a combination of time-domain signals with different amplitudes and frequencies, the time transient analysis is employed to measure the wave blocking capabilities of SMs subject to real seismic wave excitations (i.e., public earthquake data) [10, 41, 42]. This method offers an alternative perspective on the practical applicability of SMs.

1.3. Current limitations and contribution of the present study

Unlike the bandgap analysis, both the frequency domain and time transient analyses focus on the entire SM involving multiple unit cells. This necessitates greater computational resources, particularly for time transient analysis, as actual seismic wave data often comprise time-domain signals with very small-time increments. Therefore, current SM design and optimization often prioritize bandgaps, lacking discussions on the interrelationship of unit cell configurations, bandgaps, and multi-domain responses in terms of the balance between the computational complexity and performance assessment accuracy. Such a gap is unable to provide insightful guidance for effective SM design. Once the above challenges associated with the SM design can be well tackled, the underlying concept of SMs can then be broadly applied to the design of various metamaterials, demonstrating great potential for managing vibration and noise control in construction and railway environments.

The overarching goal of this research is to fill the abovementioned gap and provide profound insights and guidance for effective SM design. Specifically, in Section 2, to address the challenges faced in the design of embedded SMs, this research introduces a novel embedded SM with local resonators composed of nested cylindrical steel columns and rubber connectors. A bandgap analysis is conducted to uncover its bandgap generation mechanism, followed by the frequency domain analysis (FDA) and time transient analysis to examine the wave attenuation performance of the proposed SM.

In Section 3, using this SM as a reference, we perform the correlation study that combines bandgap analysis, FDA, and time transient analysis to comprehensively study the influence of geometric and material parameters of the unit cell on the wave attenuation performance of the synthesized SM. The interrelation among the performance indicators is also thoroughly investigated to understand the underlying characteristics of the seismic wave propagation. Section 4 is devoted to conclusions.

2. Model Development and Performance Evaluation

This section begins with the design and modeling of the embedded SM and its unit cells, followed by the introduction of bandgap analysis, frequency domain analysis (FDA), and time transient analysis to evaluate the bandgap and multi-domain characteristics of the SM. The interrelationship among the analysis results is also discussed to gain insights that will inform the appropriate selection of performance indicators for SM design, tailored to the specific operational context.

2.1. Embedded SM unit cell design

In this research, we propose a steel-rubber embedded local resonator as the main part of the SM unit cell. As illustrated in Fig. 1, this unit cell comprises a soil substrate and resonator composed of inner and outer steel columns with cylindrical cross sections, connected by rubber connectors. Apart from performance considerations, the primary rationale for choosing steel and rubber as raw materials to synthesize the SM in this research is that both steel and rubber are widely utilized and recyclable construction materials, with available waste recycling technologies [43-45]. In contrast to the general embedded local resonators discussed in Section 1, this design divides the local resonator into two components, namely the inner steel column and the outer steel column, with rubber connectors placed at the bottom and at half the height of the inner column, providing flexible constraints. The space between the two columns also allows for the vibration of the inner column. The lattice constant a is equal to 2 m, and other associated geometric parameters with descriptions are detailed in Table 1. It should be noted that the geometric parameters, including the lattice constant, the height of the local resonator and the thickness of the columns in this study are referenced within the range of values reported in the literature [14, 22, 24-29, 39, 46].

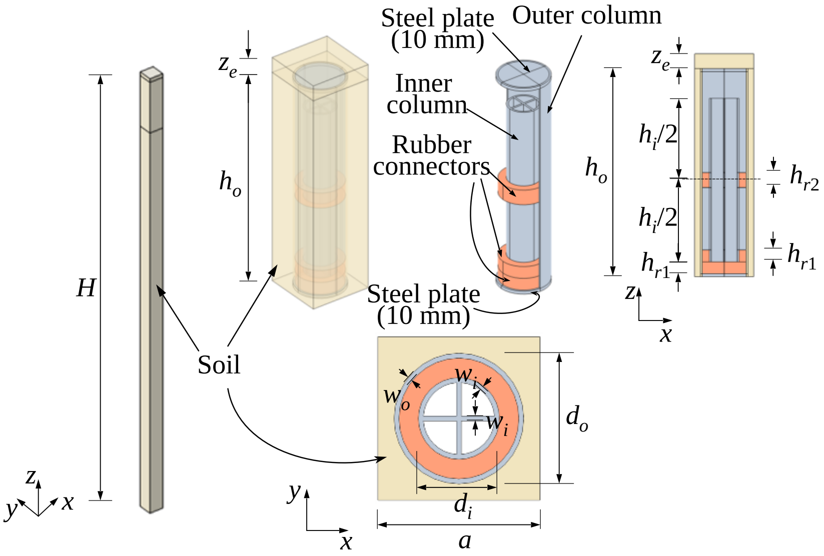

Figure 1. The configuration of the SM unit cell.

Table 1. Geometric parameters of the SM unit cell.

Parameter	Value	Description
a	2 m	Lattice constant
h_o	7 m (3.5a)	Outer column height
d_o	1.6 m (0.8a)	Outer diameter of the outer column
w_o	0.06 m (0.03a)	Outer column thickness
h_i	5.5 m (2.75a)	Inner column height
d_i	1 m (0.5a)	Outer diameter of the inner column

w_i	0.06 m $(0.03a)$	Inner column thickness
t	0.1 m $(0.05a)$	Thickness of top and bottom steel plates
h_{r1}	0.4 m $(0.2a)$	Thickness of the bottom rubber connector
h_{r2}	0.5 m $(0.25a)$	Thickness of the mid rubber connector
H	60 m $(30a)$	Soil thickness
z_e	0.5 m $(0.25a)$	Embedded depth of the local resonator

The primary purpose of using rubber between the steel columns in the local resonator is to establish soft coupling between the resonator's components, thereby generating the local resonance effect specifically for unit cells embedded underground. The unit cell design utilizing this concept and its effectiveness will be demonstrated in the subsequent section.

2.2. Bandgap evaluation

Recall the discussion in Section 1. The arrangement periodicity allows one to analyze the bandgap characteristics of the SM, providing bandgap information for initial SM design. Based on the *Bloch-Floquet theorem* [9, 24], the band structure of an infinite periodic SM can be reduced to one single unit cell with the periodic boundary condition, given as

$$\mathbf{u}(\mathbf{r}+\boldsymbol{a},t)=e^{i\mathbf{k}\cdot\mathbf{a}}\mathbf{u}(\mathbf{r},t) \tag{1}$$

where $\mathbf{u}$ denotes the displacement vector, $\mathbf{r}$ is the position vector, and $\mathbf{k}$ is the Bloch wavevector within the range of the first Brillouin zone. t represents time, and $\mathbf{a}=(a_x,a_y)$ is the lattice constant vector. a_x and a_y are lattice constants along the *x* and *y* directions in a 2D plane, respectively. For a square lattice, they are both equal to the lattice constant denoted as a in this study.

Due to the periodic boundary condition, by solving the following eigenvalue equation of one representative unit cell, one can capture the bandgap of the entire SM [39]:

$$\left(\boldsymbol{\Omega}(\mathbf{k}) - \omega^2\mathbf{M}(\mathbf{k})\right)\mathbf{u} = \mathbf{0} \tag{2}$$

where $\boldsymbol{\Omega}$ and $\mathbf{M}$ are the stiffness and mass matrices of the unit cell, respectively, with respect to the wavevector $\mathbf{k}$. ω is the angular frequency.

The dispersion curves can be derived through Eq. (2), which reflect the relation between ω and $\mathbf{k}$. To consider all wave propagation modes in all directions, the wavevector $\mathbf{k}$ should be changed across the first irreducible Brillouin zone (Γ-X-M), as shown in the gray area in Fig. 2(a). For a given wavevector without corresponding frequencies, it is termed the bandgap. Within the bandgap range, the wave cannot transmit theoretically. The finite element (FE) method software *COMSOL Multiphysics* is utilized to solve the abovementioned eigenvalue equation as described by Eq. (2). To validate the accuracy of the modeling approach, we compare the bandgap results from the present model with those reported in previous studies. Su et al. [26] designed a column-type unit cell composed of an *N*-shaped column and soil substrate, and investigated the bandgap of this unit cell. Zeng et al. [40] proposed an embedded SM unit cell, where the local resonator was composed of a steel core wrapped with foam, and experimentally assessed its wave attenuation performance. Using the modeling approach in our study, we constructed the unit cell models from the aforementioned studies, with the results depicted in Figs. 2(b) and (c), respectively. The dispersion curves in the results include both the bulk wave and surface wave modes. To identify surface wave modes, the sound cone method [47-49] is utilized. A sound line, as highlighted in red in Figs. 2(b) and (c), is used to divide the dispersion curves into two regions. The sound line is governed by the formula $\omega = \mathbf{k} \cdot c_s$, where $c_s = \sqrt{G/\rho}$ is the shear wave velocity in the soil, and G is the shear modulus [16]. Since the surface wave velocity is smaller than that of the bulk wave, the surface wave modes can be extracted in the region below the sound line. As can be seen, the dispersion curves and related bandgaps from the present model are consistent with those in [26, 40], thus thoroughly verifying the modeling approach adopted in this study.

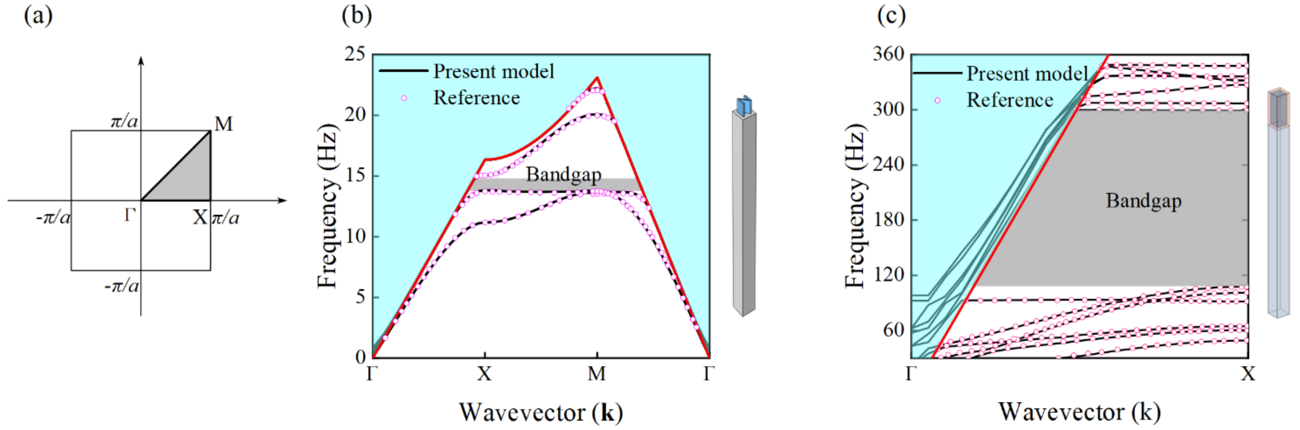

Figure 2. (a) The first irreducible Brillouin zone highlighted in gray color. Dispersion curve and bandgap identification and comparison from the unit cell models in existing studies: (b) *N*-shaped column-type unit cell [26]; (c) Embedded unit cell [40].

Following the initial idea guiding the unit cell design outlined in Section 2.1, the rationale behind the unit cell configuration design and its effectiveness have been further clarified in Appendix A. With this understanding, we finalize the unit cell configuration and establish its finite element (FE) model, as shown in Fig. 3(a). Periodic boundary conditions are applied to the four sides of the cell, and the bottom of the soil layer is fixed [27, 50]. The materials in the model are assumed to be homogeneous, isotropic linear elastic materials [28, 30], which is an essential assumption for seismic wave propagation to facilitate the bandgap calculation. The mass densities of the soil, steel, and rubber are 1,800, 7,850, and 1,300 kg/m^3, respectively, with Young's moduli of 20, 2.1×10^5, and 1 MPa, and Poisson's ratios of 0.3, 0.3, and 0.47, respectively. The analysis results are shown in Fig. 3(b). The results indicate that three individual bandgaps are observed, ranging from 3.78 to 4.34 Hz, 5.0 to 8.33

Hz, and 9.29 to 16.37 Hz, respectively, with a total width of 10.97 Hz. The total bandgap width accounts for 67% of the region below the sound line.

To further investigate the mechanism of bandgap generation, three typical modal points (A1, A2 and A3 in Fig. 3(b)), located at the lower boundaries of the first, second, and third bandgaps, respectively, are extracted with corresponding mode shapes depicted in Fig. 4. Note that the arrows in Fig. 4 represent the resonance directions of the unit cell. It is observed that point A1 exhibits bending resonance of the inner column, with the modal displacement amplitude located at the top of the column. Point A2 corresponds to the torsional resonance mode of the inner column. Point A3 also shows the bending resonance of the inner column. Differing from point A1, the resonance concentrates at the bottom of the inner column. Interestingly, the resonance of the outer column is almost imperceptible, as it is constrained by the surrounding soil. Based on the results, it is observed that for the mode shapes at the first and second bandgap upper boundaries (points B1 and B2 in Fig. 3(b)), the maximum modal displacement is primarily concentrated at the resonator, with the inner column exhibiting vertical and lateral bending resonance, respectively. The parts of the soil substrate are involved in the vibration, which is consistent with the findings reported by Zhang et al. [46]. Furthermore, the upper edge of the third bandgap is located at the upper boundary of the sound line region, with the vibration mainly located at the soil substrate, identical to the observations in [24]. The analysis results also indicate that due to the flexible constraints by the rubber connectors, with sufficient space reserved between the inner and outer columns, the local resonance of the inner column remains almost unrestricted. As a result, it leads to the generation of wide low-frequency bandgaps.

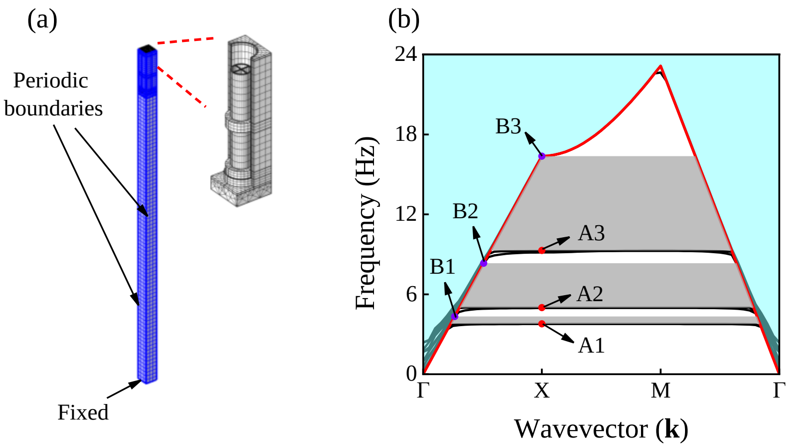

Figure 3. (a) The unit cell finite element (FE) model for bandgap analysis; (b) Bandgap results of the developed unit cell shown in Fig. 1.

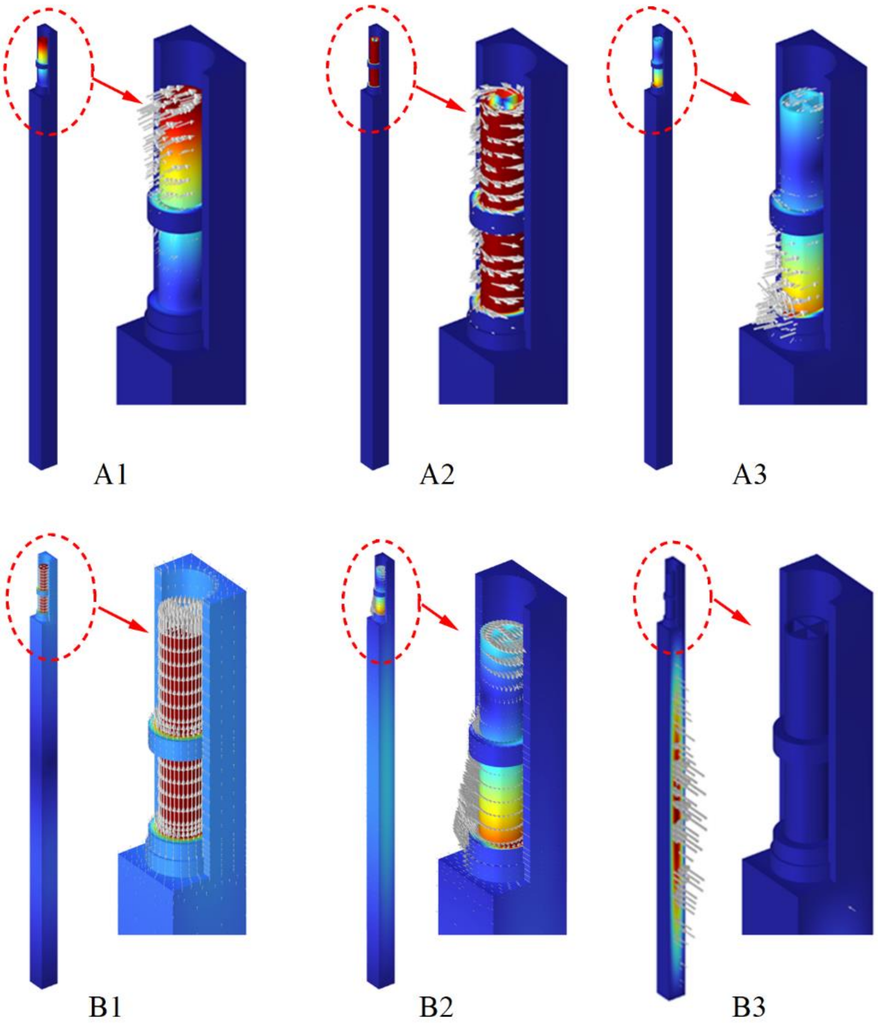

Figure 4. Mode shapes at the lower and upper boundaries of bandgaps. A1, A2, and A3 are located at the lower boundaries of the first, second, and third bandgaps, respectively. B1, B2, and B3 are

located at the upper boundaries of the first, second, and third bandgaps, respectively.

2.3. Frequency domain analysis

In theory, the propagation of seismic waves within bandgap ranges would be completely blocked by SMs, but this assumes of the fully periodic unit cell arrangement, which is unattainable in practical applications. Furthermore, while the bandgap informs the frequency range where seismic waves can be theoretically attenuated by the SM, it fails to indicate the degree of the wave mitigation, i.e., amplitude reduction. For these reasons, it is necessary to further evaluate the wave attenuation performance of the SM through frequency domain analysis (FDA). The FDA model used in our study is illustrated in Fig. 5. The seismic wave propagates along the positive x-axis, with 15 unit cells arranged in this direction. A line source is located on the left side of the SM, with a frequency-sweeping harmonic excitation used to generate excitation waves as input, and the displacement amplitude on the right side of the SM is recorded as output [42, 51, 52]. The distance between the excitation and the SM is set to $10a$ to ensure that only surface waves interact with the SM, as surface waves carry the majority of the energy that is concentrated at the soil surface and dissipates rapidly with the soil depth [27]. Additionally, a special boundary condition, known as the *perfectly matched layer* (PML) with a thickness of $3a$, is applied at the bottom and two sides of the model to minimize unwanted wave reflection [46, 49]. To reduce computational time, periodic boundary conditions are applied in the direction along the y-axis [24, 30]. For all FE models in this research, the maximum element size is selected as 0.65 m, which is ensured to be smaller than 1/5 of the minimum surface wavelength [16, 27, 39]. The numerical simulations are deployed on a computer with an Intel i7 13700 CPU. The time required for FDA is approximately 10.3 hours.

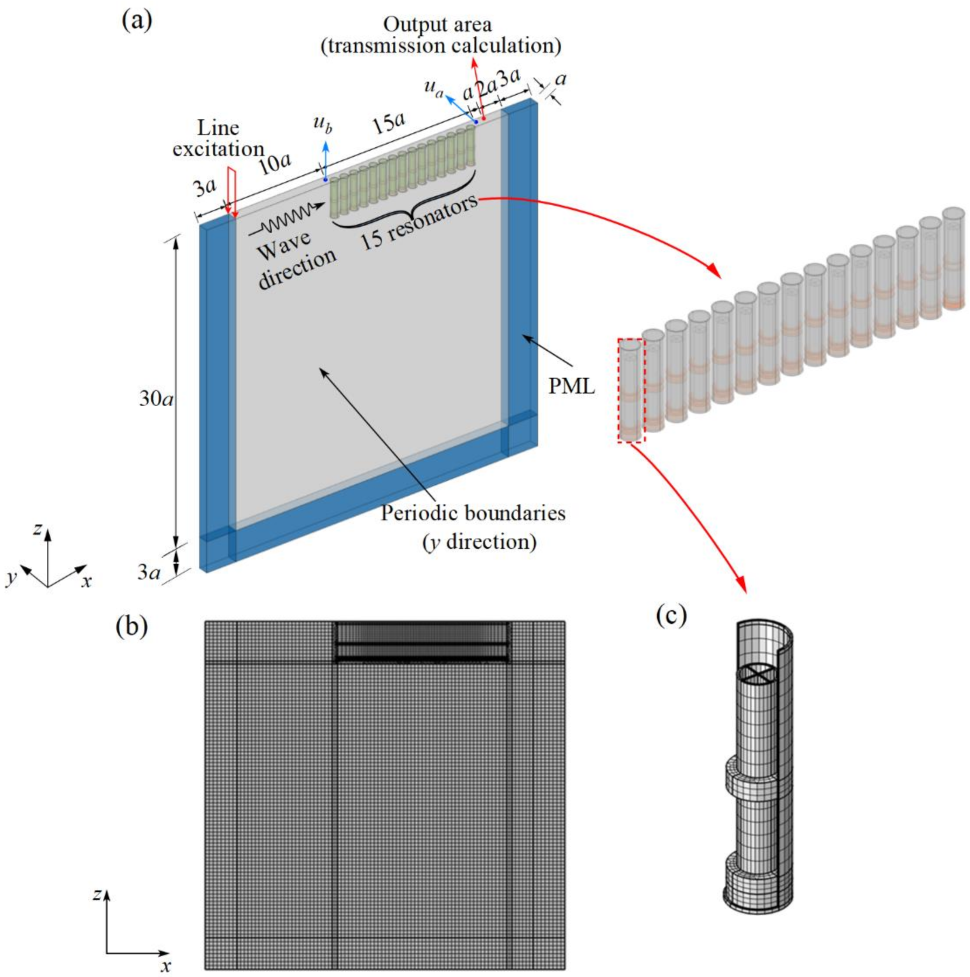

Figure 5. Frequency domain analysis (FDA) model: (a) Three-dimensional FDA model with 15 unit cells; (b) Global mesh; (c) Mesh of the local resonator.

Transmission, a widely utilized metric to evaluate wave attenuation using FDA, can be calculated by the following equation [30, 53]:

$$T(f) = 20\log_{10}\left(\frac{u_1(f)}{u_2(f)}\right) \tag{3}$$

where $T(f)$ is the transmission at the frequency f. $u_1(f)$ and $u_2(f)$ are the displacement amplitudes at the output area obtained from the models with and without the SM, respectively. Clearly, a negative value of $T(f)$ indicates that the seismic wave with the frequency of f is attenuated. The smaller the $T(f)$, the better the wave attenuation capability of the SM at the corresponding frequency.

Fig. 6 illustrates the transmission result, alongside the bandgap information for comparison. It can be found that the wave attenuation zones of the transmission match closely with the bandgap distribution. In the second bandgap range, the maximum attenuation of seismic waves reaches approximately 35 dB, further illustrating the effectiveness of this SM. However, it should be acknowledged that such agreement may not hold when the SM configuration is set differently. It is hence worth exploring the key characteristics of dispersion curves and transmissions in relation to the SM configuration, which aims to gain a deep understanding of how their relationship changes with alterations to the SM configuration.

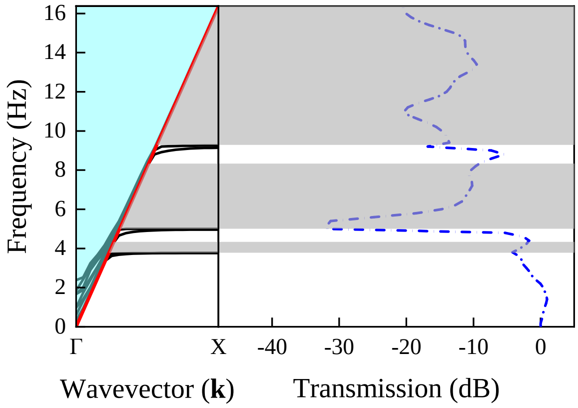

Figure 6. Comparison between the bandgaps and transmission. (Gray areas denote bandgaps)

In addition to transmission, another indicator, namely wave reduction factor, is adopted to assess wave attenuation provided by the SM. This indicator is expressed as follows [33, 37]:

$$R(f) = 20\log_{10}\left(\frac{u_a(f)}{u_b(f)}\right) \tag{4}$$

where $u_a(f)$ is the displacement value at the position after the SM at frequency f, and $u_b(f)$ is the displacement value at the position before the SM at the same frequency.

Given the deterministic locations for assessment, we can calculate the $R(f)$ of the models with and without the SM, respectively Using Eq. (4), and compared the results, as depicted in Fig. 7. The results indicate that when the SM is not deployed, the $R(f)$ value is close to zero, indicating minimal attenuation of seismic surface waves. In contrast, with the SM consisting of 15 unit cells arranged in the wave propagation direction, significant wave attenuation is observed in the bandgap regions after passing through the unit cell array in the SM. The attenuation performance is especially excellent in the second and third bandgap regions. As a comparison, within the frequency range of the first bandgap, inferior wave attenuation is noticed. We also compare the transmission and the wave reduction factor obtained from the FDA model considering the SM deployment, as illustrated in Fig. 8. The results show that the two frequency domain metrics match very closely.

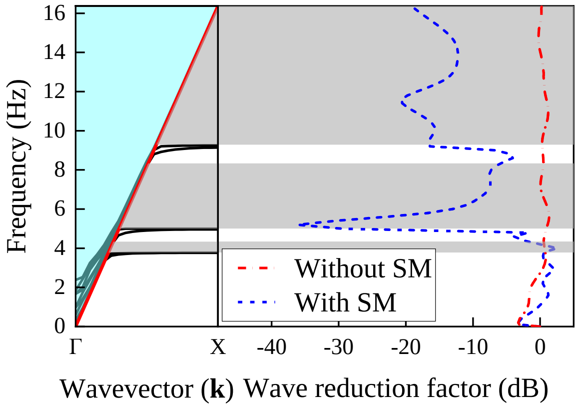

Figure 7. Comparison between the bandgap and wave reduction factors with and without the SM. (Gray areas denote bandgaps)

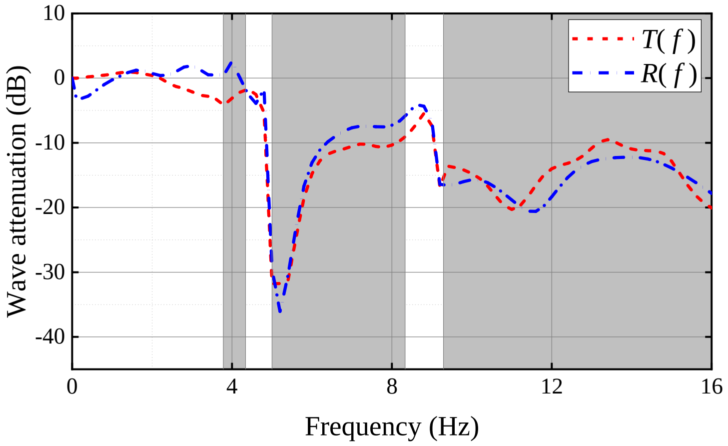

Figure 8. Comparison between the transmission and the wave reduction factor when the SM is involved. (Gray areas denote bandgaps)

2.4. Time transient analysis

As outlined in Section 1, FDA reveals the response of the SM under a harmonic excitation, providing a quantitative assessment of the SM performance under varying frequencies. It is noted that seismic waves in reality are time-domain excitations, encompassing components with different amplitudes and frequencies. Therefore, time transient analysis is adopted to assess the attenuation of actual seismic waves yielded by the SM in the time domain. This type of analysis is particularly suited to accommodating publicly accessible earthquake-induced ground motion data, which favors validation in a more realistic context. The same SM configuration with unit cells engineered in Section 2.3 is investigated in this time transient analysis. The numerical model constructed resembles the one shown in Fig. 5, with the difference being that, the *perfectly matched layer* (PML) is replaced by a low-reflective boundary as it cannot be used in time transient analysis [24, 39, 54]. In this section, *Landers earthquake* [55] (Fig. 9(a)), *Kobe earthquake* [56] (Fig. 9(b)), *Oroville Dam earthquake* [57] (Fig. 9(c)), and *Anza earthquake* (Fig. 9(d)) [58] acceleration data are adopted as the input signals in analysis, respectively. The four acceleration signals are downloaded from PEER ground motion database. In addition, we also establish a model without the SM to compare the differences in seismic response, i.e., acceleration time history at the output area. The average time of time transient analyses for the Landers, Kobe and Anza earthquakes is approximately 23.1 hours, while it is approximately 10.2 hours for the Oroville Dam earthquake. Figs. 10(a)-(d) show the output acceleration responses with and without the SM under the four earthquakes. It can be observed that the peak acceleration response at the output area with the SM is significantly reduced compared to that without the SM. Figs. 11(a)-(d) present the Fourier spectra of the output acceleration responses, with gray areas indicating the bandgaps. Clearly, within the bandgap ranges, the output acceleration amplitude observed in the Fourier spectra is substantially reduced for the model with the SM.

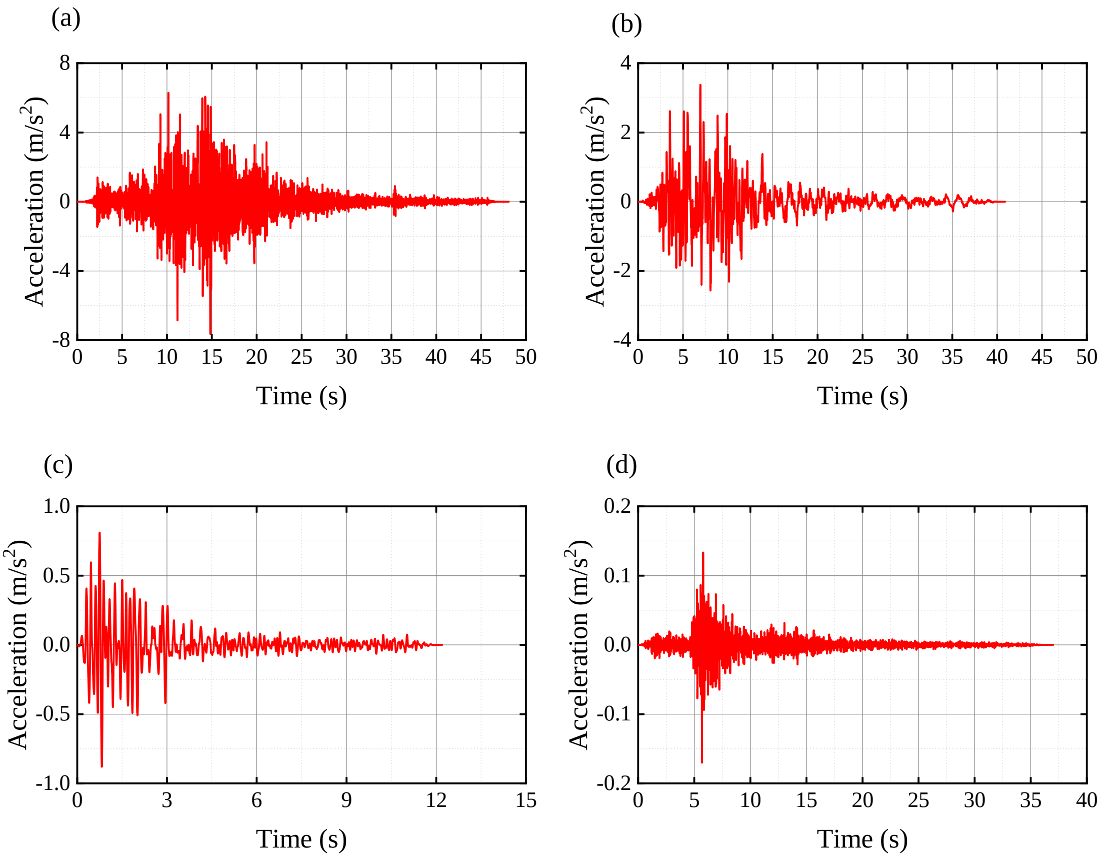

Figure 9. The actual seismic wave signals in time transient analyses: (a) Landers earthquake; (b) Kobe earthquake; (c) Oroville Dam earthquake; (d) Anza earthquake.

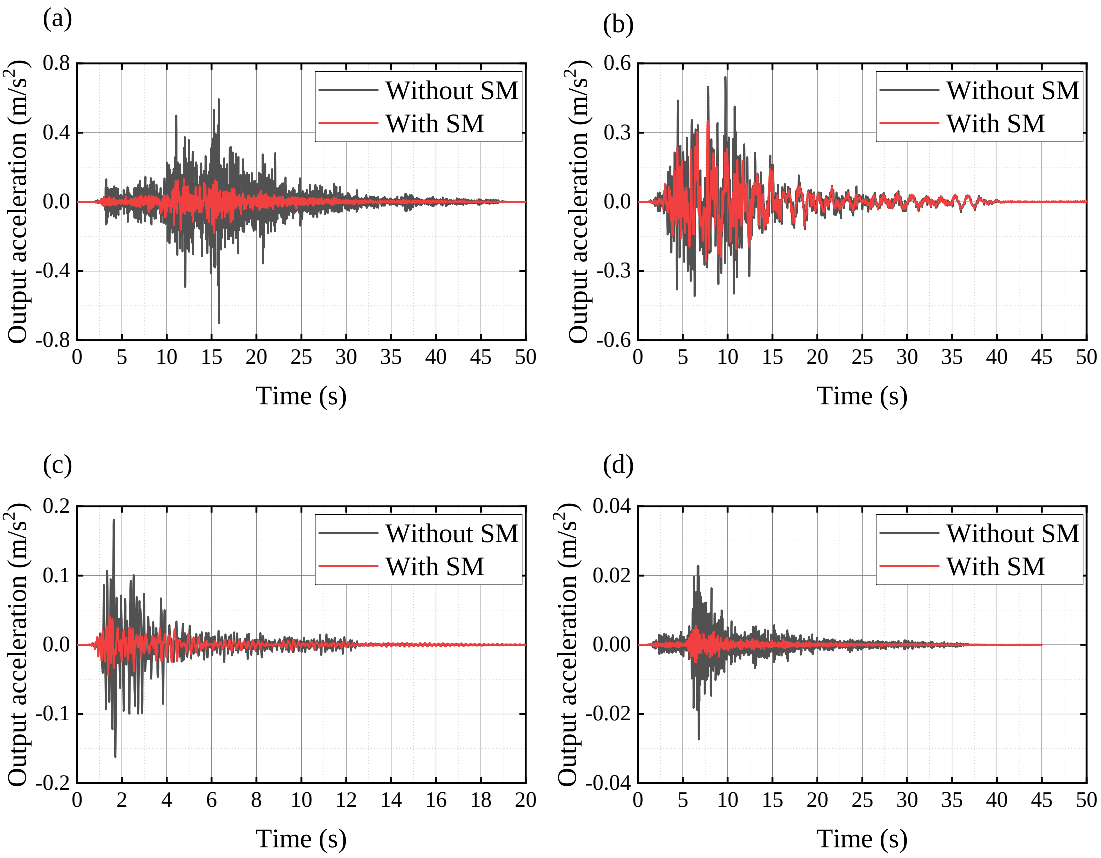

Figure 10. The output acceleration time histories: (a) Landers earthquake; (b) Kobe earthquake; (c) Oroville Dam earthquake; (d) Anza earthquake.

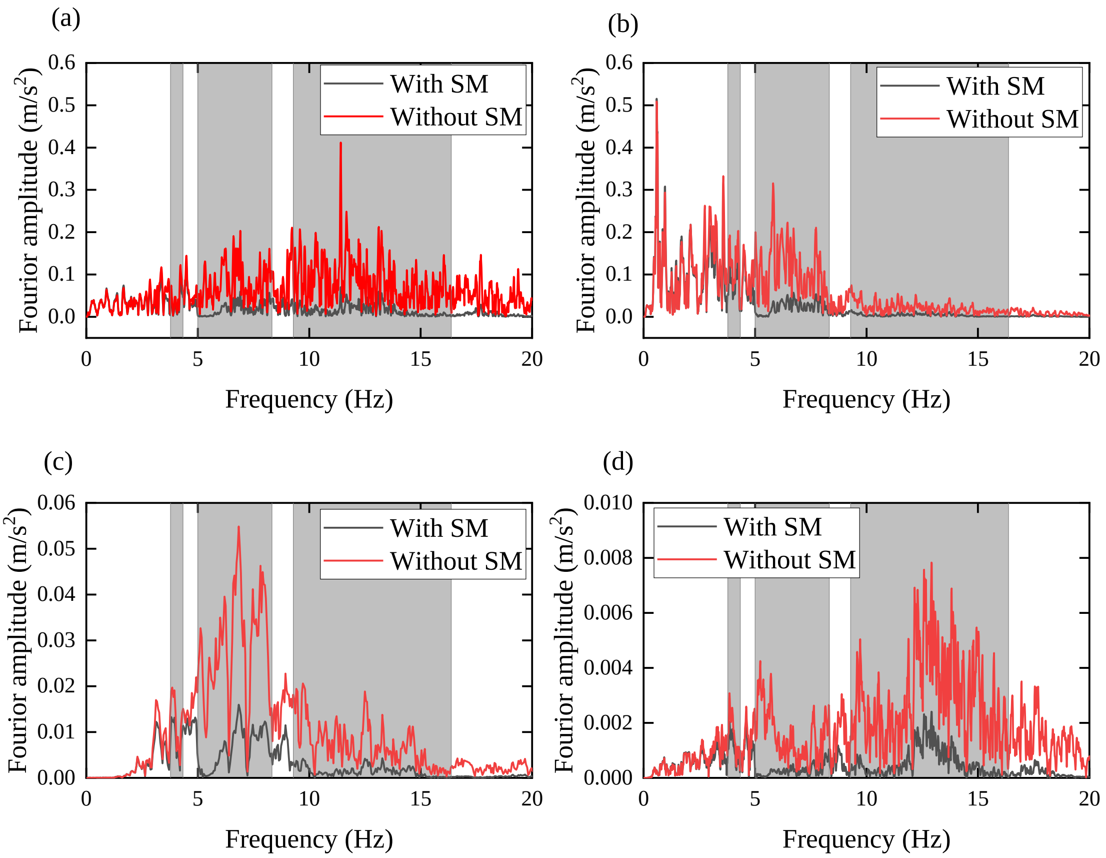

Figure 11. Fourier spectra of the output acceleration data: (a) Landers earthquake; (b) Kobe earthquake; (c) Oroville Dam earthquake; (d) Anza earthquake. (Gray areas in (a)-(d) denote bandgaps)

For a comparable investigation, based on the obtained Fourier spectra of output responses, we defined an indicator similar to the transmission in FDA as follows:

$$A(f) = 20\log_{10}\left(\frac{a_1(f)}{a_2(f)}\right) \tag{5}$$

where $A(f)$ is the attenuation spectrum calculated through the Fourier spectra, i.e., $a_1(f)$ and $a_2(f)$ that represent the response amplitudes at the output area with and without the SM, respectively.

Fig. 12 presents a comparison between the transmission results derived from frequency domain analysis (FDA) and the attenuation spectra from time transient analysis. The attenuation spectra, generated under the Landers, Kobe, Oroville Dam, and Anza earthquake-induced ground motion, show a high degree of consistency. Furthermore, there is a strong correlation between the transmission and attenuation spectra, with minor differences potentially arising from the boundary conditions of the model. Similar to the transmission, noticeable reductions in attenuation spectra are captured within the bandgap ranges. In the following study, the intercorrelation among bandgaps, and the frequency-domain and time-domain responses will be further investigated to acquire more comprehensive insights.

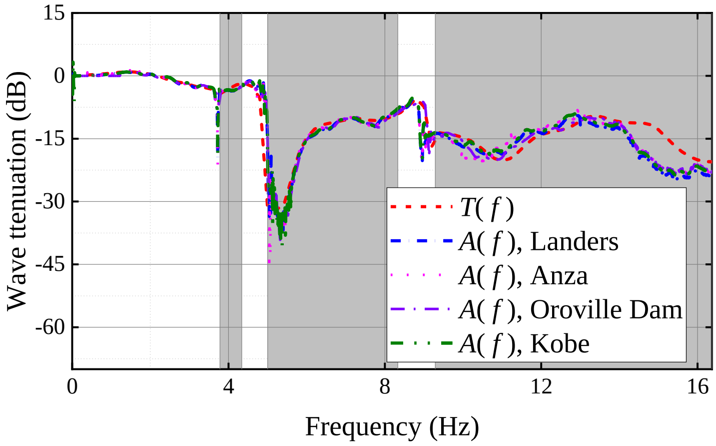

Figure 12. The comparison among the bandgaps, transmission from FDA, and attenuation spectra from time transient analyses. (Gray areas denote bandgaps)

3. A correlation Study to Reveal Underlying Seismic Metamaterial Behaviors

It is evident that the geometry and material properties of the SM can influence the seismic wave attenuation performance. In order to comprehend the complex wave propagation to benefit the SM design, it is necessary to conduct parametric investigations using the combined bandgap analysis and multi-domain performance evaluation. This will help elucidate the intrinsic correlation among the unit cell configuration and multi-domain characteristics, such as the attenuation behavior in the time transient analysis, transmission in the frequency domain, and bandgap. Specifically, the unit cell configuration is represented by three main parameters, including the height of the fully embedded resonator, stiffness of connectors in the fully embedded resonator, and resonator embedded depth. These parameters serve as representative and cost-effective design variables in general SM design problems.

3.1. Elucidating correlation in terms of the height of the fully embedded resonator

It is noteworthy that the height of the local resonator is defined by the height of the outer column. (i.e., h_o in Fig. 1 and Table 1). Moreover, the height discrepancy between the outer and inner columns is maintained as a constant value (i.e., $h_o - h_i = 0.75a$), and rubber connectors are positioned at the midpoint of the inner column, irrespective of any variation in the height of the outer column. In this investigation, 11 height values ranging from $3.5a$ to $8.5a$ are sampled with the increment of $0.5a$ and then cast into the analysis to compute their bandgaps. Fig. 13(a) demonstrates how changes in the height of the local resonator influence the bandgaps. As the result shows, when increasing the resonator height, the lower boundaries of the first, second, and third bandgaps decrease. This is likely due to the reduction in axial stiffness of the inner column as its height grows. In general, there is a positive correlation between the resonator height and the overall width of the bandgaps. Specifically, as the height of the resonator increases, the overall bandgap width widens from 10.97 Hz to 12.89 Hz, with the expansion of the third bandgap making a significant contribution. 6 representative bandgaps associated with resonator heights escalating from $3.5a$ to $8.5a$ in the increment of $1.0a$ are retrieved from Fig. 13(a). As previously noted, bandgaps serve as an ideal metric for reflecting the intrinsic behavior of the SM. Given that bandgaps are not directly measurable, conducting comprehensive performance evaluation of the SM requires examining the intrinsic relationship between the bandgap and multi-domain characteristics of the SM. Therefore, the frequency domain metrices, including the transmission ($T(f)$) and wave reduction factor ($R(f)$), are subsequently evaluated using FDA. Beyond this, we also conduct time transient analyses under Landers earthquake acceleration data, and calculate the attenuation spectra ($A(f)$) corresponding to unit cell configurations with different resonator heights. The comparative analyses and relevant results are illustrated in Figs. 13(b)-(g). The results demonstrate good agreement between the bandgaps and the zones indicating significant wave reduction in transmissions, wave reduction factors and attenuation spectra across all 6 cases, especially within the second and third bandgaps. The results also reveal that while the distribution of bandgaps shifts with changes in resonator height, the overall features of the dispersion curves remain consistent across different heights. For instance, the number of bandgaps remains the same despite variations in resonator height. Moreover, it is interesting to find that the upper limit of the third bandgap consistently aligns with the boundary of the sound line region, specifically at 16.37 Hz.

As the height of the resonator rises, there is a more pronounced decrease observed in transmissions, wave reduction factors and attenuation spectra, particularly within the frequency range of the third bandgap. To elucidate this effect, we extract the displacement field from the FDA at a frequency of 11.8 Hz, where the transmission reaches -39 dB with the resonator height specified as $4.5a$. The result is illustrated in Fig. 13(h). Interestingly, the comparison between Fig. 13(b) and Fig. 13(g) indicates that the seismic wave attenuation does not significantly elevate as expected when the height continues to rise from $4.5a$ to $8.5a$, in the third bandgap region. The possible reason is that the third bandgap originates from the local resonance of the inner column, which is most pronounced near the bottom of the column. If the resonator height becomes excessive, the bottom of the column is positioned too distant from the topsoil. Given that the energy of seismic surface waves is predominantly concentrated near the ground surface, an overly tall inner column may not effectively dissipate seismic energy as anticipated. This indicates the existence of an optimal resonator height that balances performance with cost, given the fact that the manufacturing expenses of the SM increase with the height of the resonators. While significant vibration reduction is achieved within the bandgap regions of multi-domain responses, clear distinctions between bandgap and multi-domain characteristics can still be recognized. Depending solely on bandgap analysis may not adequately reflect the relationship between the height of the resonators and the degree of seismic wave attenuation. On the other hand, a more reliable and thorough assessment can be conducted by combining bandgap analysis with multi-domain analyses. Additionally, comparative studies show that the results of time domain analysis and FDA (including transmission and wave reduction factor) exhibit a high degree of consistency. This indicates that the frequency domain transmission can serve as an alternative to the time domain indicator, especially considering the increased computational demand of the time transient analysis. Based upon this finding, we will adopt transmission as the SM performance metric in subsequent investigations to facilitate the computational design with enhanced efficiency. The following cases will not include a direct comparison or discussion of the results from time transient analysis and frequency domain analysis (FDA).

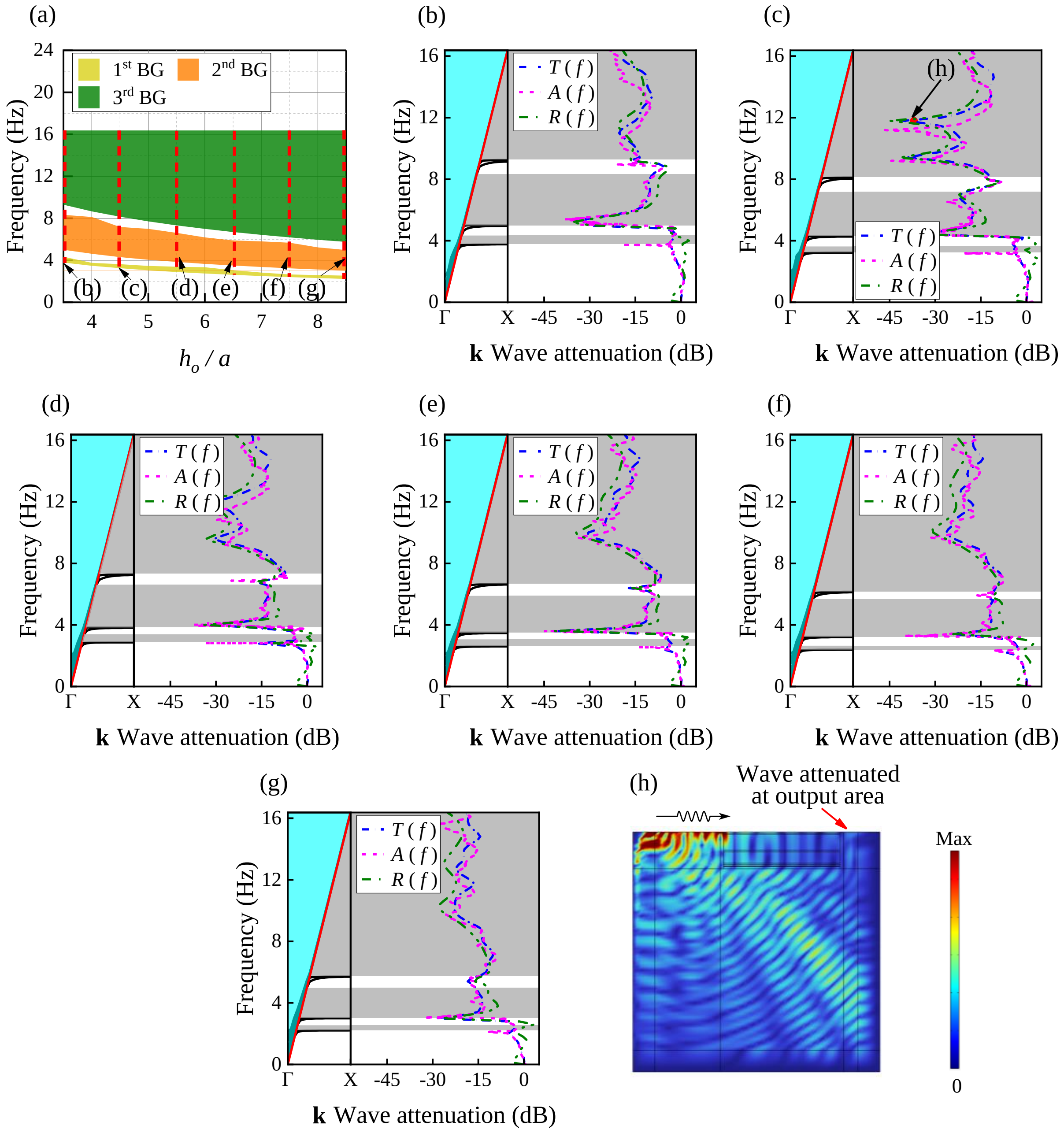

Figure 13. Correlation analysis results of the resonator height (h_o): (a) Bandgaps (BG denotes the bandgap); (b) $h_o = 3.5a$; (c) $h_o = 4.5a$; (d) $h_o = 5.5a$; (e) $h_o = 6.5a$; (f) $h_o = 7.5a$; (g) $h_o = 8.5a$; (h) Displacement field in the FDA model ($h_o = 4.5a$, 11.8 Hz). (Gray areas in (b)-(g) denote bandgaps)

3.2. Elucidating correlation in terms of the stiffness of connectors in the fully embedded

resonator

Section 2.2 highlights the role of connectors in providing flexible constraints to the inner column, enabling the generation of local resonance, and thus resulting in low-frequency bandgaps. Nevertheless, the impact of the coupling degree between columns, as influenced by these constraints, on wave attenuation performance has not been quantified. In this subsection, we increase the connector stiffness by adjusting the Young's modulus of connectors across a range of 11 values, from 1 to 26 MPa with the increment of 2.5 MPa, and then conduct the quantitative examination. The resulting bandgaps are analyzed and presented in Fig. 14(a). It can be observed that the lower boundaries of the bandgaps shift upwards as Young's modulus of connectors increases from 1 to 11 MPa, due to the enhanced constraint of the internal column imposed by the connectors. The results also demonstrate the high sensitivity of bandgaps to the connector stiffness, with a rise in stiffness leading to a reduction in the total bandgap width. Notably, when the Young's modulus of connectors reaches 26 MPa, the bandgaps are no longer observed due to the stronger restriction imposed by the elevated connector stiffness. In other words, the rigid coupling in this extreme case eliminates the possibility of the relative motion between the inner and outer columns, and thus disables the local resonance effect when the local resonator is completely restricted by the surrounding soil.

Comparisons of transmissions and bandgaps under typical connector stiffness values are also presented in Figs. 14(b)-(g). When the Young's modulus of connectors is low, only minor differences are captured between the bandgaps and attenuation zones in the transmission. However, as the Young's modulus of connectors increases, these discrepancies become more pronounced, primarily as a result of the significant alterations in dispersion curves and bandgaps. It is surprisingly noted that the bandgaps are no longer present at Young's modulus of 26 MPa. Despite this, attenuation of seismic waves is still evident in the transmission. Fig. 14(h) depicts the displacement field at the frequency of 15.2 Hz with the Young's modulus of 26 MPa. As a result of the reflection and refraction between different media, the surface wave is converted to the bulk wave when passing through the SM, aligning with the results reported by Wang et al. [59]. Furthermore, the comparison between Fig. 14(b) and Fig. 14(g) indicates that the SM with existing bandgaps demonstrates superior wave blocking capabilities within the sound line area (0-16.37 Hz). These findings underscore the practical significance of SMs that leverage local resonance in engineering applications. Additionally, the transmission accounts for many realistic influential factors, offering insights into aspects beyond merely the attenuation of surface waves, as demonstrated by the bandgap alone.

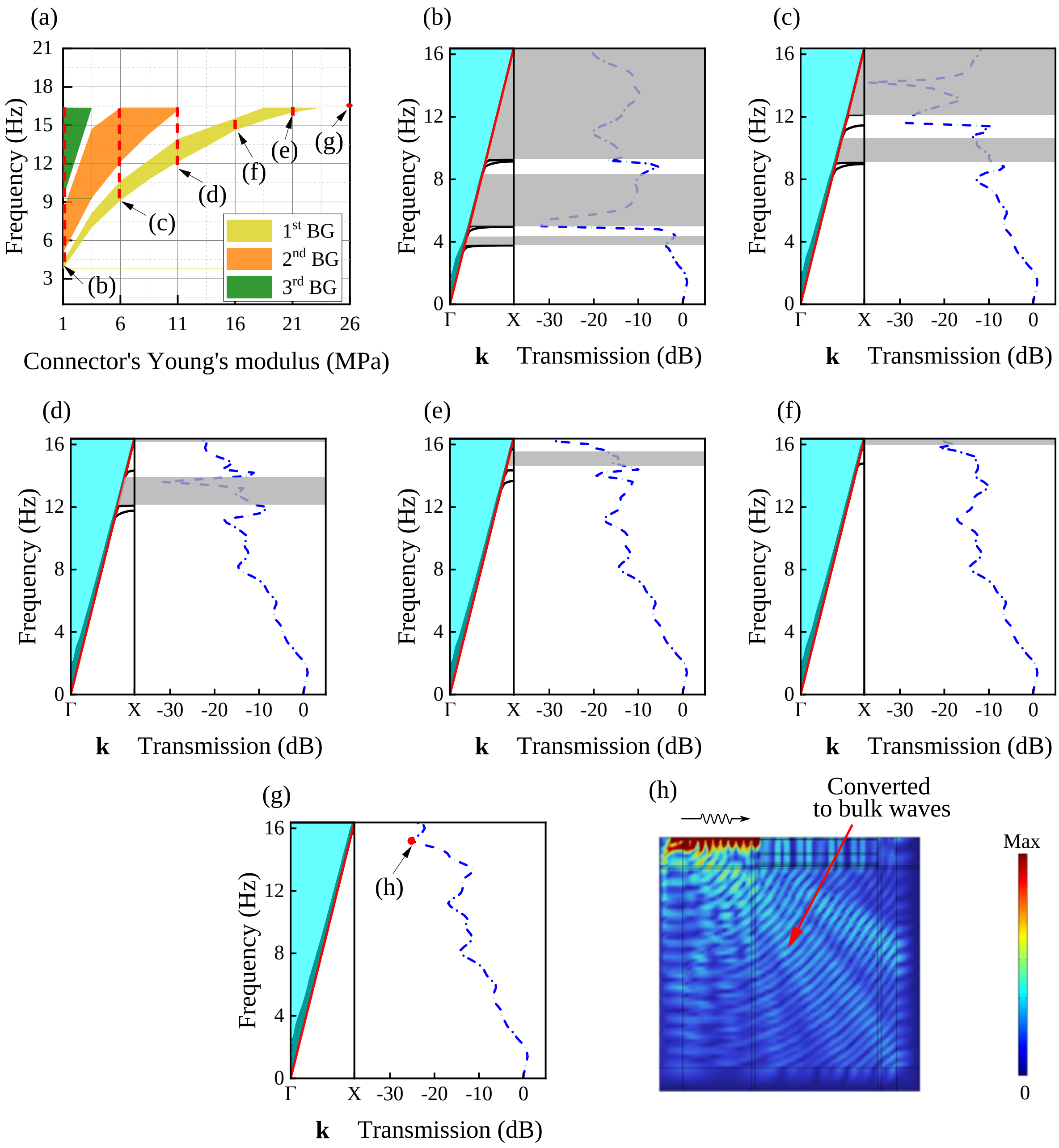

Figure 14. Correlation analysis results of Young’s modulus of the connector: (a) Bandgaps (BG denotes the bandgap); (b) 1 MPa; (c) 6 MPa; (d) 11 MPa; (e) 16 MPa; (f) 21 MPa; (g) 26 MPa; (h) Displacement field (26 MPa, 15.2 Hz). (Gray areas in (b)-(g) denote bandgaps)

3.3. Elucidating correlation in terms of the resonator embedded depth

In engineering applications, it may be necessary to modify the embedded depth of resonators to accommodate existing infrastructure, such as natural gas or water pipelines. Beyond this practical consideration, the embedded depth of resonators can also influence wave attenuation, warranting further investigations. Following similar analysis procedures outlined in Sections 3.1 and 3.2, we generate a series of 11 depth values ranging from $0a$ to $2.5a$ with the increment of $0.25a$ while maintaining a constant resonator height of $3.5a$. It is worth clarifying that the embedded depth (i.e., z_e in Fig. 1) in this context refers to the distance from the top of the outer column to the ground surface given the fully embedded resonators (shown in Fig. 1). Fig. 15(a) illustrates the varying tendency of the bandgap with respect to the embedded depth. As can be seen, bandgap widths remain visibly unchanged until the embedded depth surpasses $1.0a$. Beyond this point, the width of the third bandgap notably diminishes. When it exceeds $2.0a$, the third bandgap vanishes. The variation in embedded depth also alters the general characteristics of dispersion curves. As depicted in Figs. 15(b)-(g), when the depth is less than $1.0a$, the SM present similar type of dispersion curves, with the upper limit of the third bandgap coinciding with the boundary of the sound line area. However, as the embedded depth rises to $1.5a$, the upper limit of the third bandgap begins to shift downwards. The second and third bandgaps are more sensitive to the embedded depth than the first bandgap.

Similarly, transmissions are analyzed alongside bandgaps for comparative purposes, as demonstrated in Figs. 15(b)-(g). It becomes clear that when the embedded depth does not surpass $1.5a$, the bandgaps align well with the attenuation zones observed in the transmission. However, if the embedded depth continues to increase, even within the bandgap region, seismic wave attenuation becomes limited. Particularly, when the embedded depth is increased to $2.5a$, the attenuation of seismic waves in the bandgap region is significantly diminished compared to the case without the embedded depth, i.e., the top of the column is level with the ground. To further investigate this, we compare the displacement fields of the models with embedded depths of $0a$ and $2.5a$, respectively, at the frequency of 5.6 Hz (within the bandgap region) shown in Fig. 15(h). Clearly, the seismic wave travels directly through the SM with the embedded depth of $2.5a$, and there is no noticeable attenuation. This is attributed to the fact that the vibration energy of the seismic wave is predominantly concentrated at the topsoil. When the embedded depth is excessively large, the wave can bypass the local resonators by traveling through the topsoil above them, rendering these resonators nearly ineffective. Overall, the discrepancies between bandgaps and attenuation zones in the transmission become more evident as the embedded depth increases. This reiterates that although bandgaps provide a preliminary and ideal metric for guiding the design of SMs owing to their desired computational efficiency, they may not fully capture the intricate wave propagation behaviors in certain scenarios. Given the specific operational and deployment condition, the appropriate performance indicator should be chosen to conduct the effective SM design while minimizing the dependency on the computational resources.

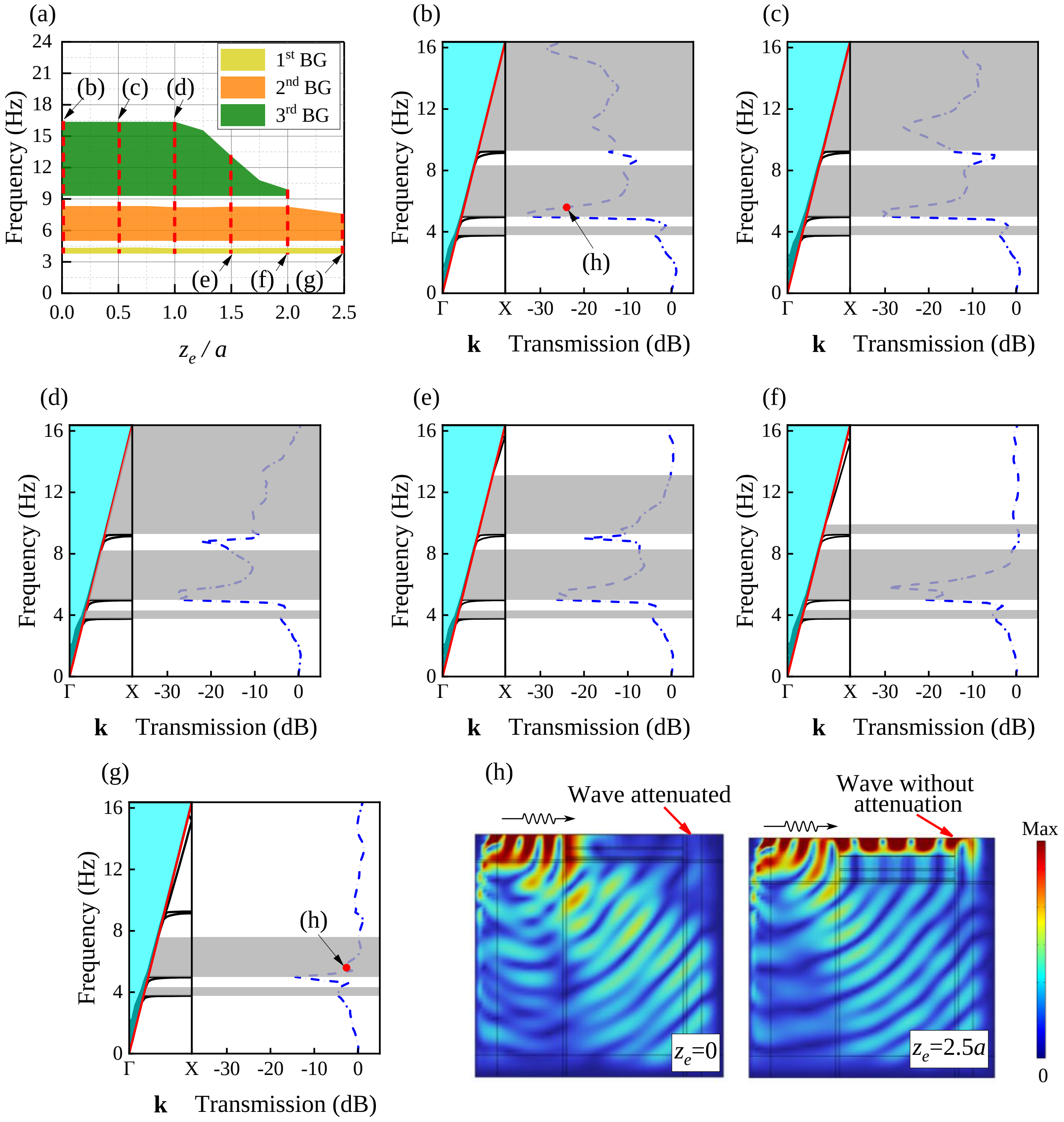

Figure 15. Correlation analysis results of the embedded depth (z_e): (a) Bandgaps (BG denotes the bandgap); (b) $z_e = 0a$; (c) $z_e = 0.5a$; (d) $z_e = 1.0a$; (e) $z_e = 1.5a$; (f) $z_e = 2.0a$; (g) $z_e = 2.5a$; (h) Displacement fields comparison (5.6 Hz). (Gray areas in (b)-(g) denote bandgaps)

4. Conclusions

In this research, we aim to shed new light on seismic metamaterial (SM) design via thoroughly exploring the intrinsic correlation between the unit cell configuration and its wave attenuation performance indicators, including both the bandgap and characteristics in frequency and time domains. A novel embedded SM with unit cells composed of soil, inner and outer steel columns, and rubber connectors is invented as the backbone of the investigation. This specific SM is environmentally sustainable, as both rubber and steel are highly recyclable materials with well-established recycling technologies. The main findings and contributions of this research encompass:

(1) The proposed embedded SM involves unit cells, each featuring a local resonator consisting of steel columns and rubber connectors. This SM configuration enhances the local resonance effect, leading to the generation of low-frequency bandgaps. The combined bandgaps have a width of 10.98 Hz, covering approximately 67% of the sound line region. The transmission and wave reduction factor results obtained from frequency domain analysis (FDA) exhibit a high level of consistency, indicating the exceptional attenuation of seismic waves, particularly within the second and third bandgap regions. The results of the time transient analysis that incorporates the actual earthquake-induced ground motion data also indicate the ability of the SM to attenuate seismic waves in real-world conditions. The attenuation spectrum derived from time transient analysis corresponds closely with the transmission from FDA, implying their interchangeable role in assessing the SM performance.

(2) Treating the proposed embedded SM as a baseline, a parametric study is conducted to uncover the inherent relationship between the unit cell configuration, bandgap, transmission, and time-domain behavior. Specifically, an increase in resonator height leads to an expansion of the total bandgap width, with the multi-domain indicators accurately reflecting the bandgap distribution. However, there may be an optimal resonator height that balances cost and performance. Although the bandgap is unable to accurately quantify wave attenuation degrees, it can still be utilized to predict the distribution of the

attenuation zone when varying resonator heights. The stiffness of connectors plays an important role in shaping the bandgaps. A highly stiff connection suppresses local resonance, resulting in the disappearance of bandgaps. In this case, the transmission cannot capture the bandgap varying tendency, which is possibly due to wave reflection and refraction across different media. Furthermore, increasing the embedded depth of the resonator tends to narrow the bandgap width, especially beyond a certain threshold. The transmission reveals the diminished capability of the SM for seismic wave attenuation, even though the frequencies of the seismic wave fall within the bandgap range.

(3) The insights obtained from this study offer valuable guidance for effective SM design. This includes optimizing unit cell configuration and selecting appropriate performance indicators, while balancing computational costs and design reliability for a specific SM and its intended deployment conditions. Although the detailed insights into the intrinsic correlation mentioned above are derived from a specific SM developed in this research, the underlying principles governing seismic wave propagation are similar across various classes of SMs. Therefore, these insights can be transferred and extended to design of other metamaterials, the outcomes of which can be potentially employed for mitigating vibration and noise from construction activities and rail transportation.

Future studies could focus on leveraging artificial intelligence (AI) to enhance SM design capabilities, integrating a broad spectrum of realistic design criteria. The utility of the insights obtained will be assessed through the results from AI-empowered design approaches.

Appendix A. Rationale behind the unit cell design

As previously mentioned, to address the restricted local resonance in embedded unit cells, soft materials are used between the components of the local resonator to resolve this issue. Inspired by this concept, an embedded unit cell is initially proposed, as illustrated in Fig. A1(a). The inner column, serving as the core of the local resonator, is encased by rubber positioned on four sides and at the base of the column. The dispersion curve for this unit cell is depicted in Fig. A2(a), indicating four bandgaps within the frequency ranges of 5.68 to 6.94 Hz, 7.47 to 12.22 Hz, 14.11 to 15.46 Hz, and 15.87 to 16.37 Hz, respectively, with a cumulative width of 7.86 Hz.

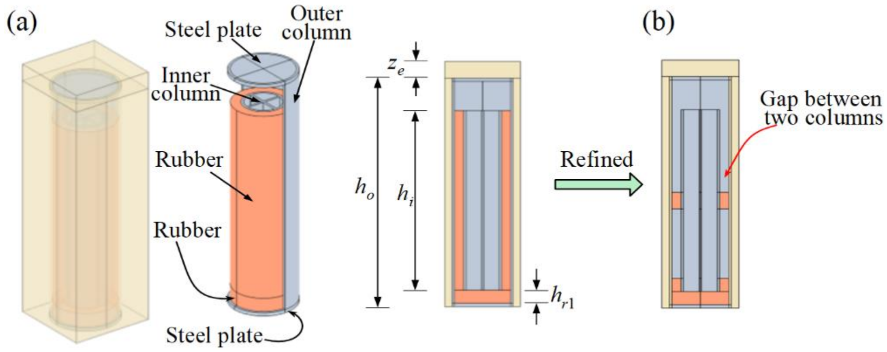

Figure A1. (a) Initially designed configuration of the embedded unit cell; (b) Refined configuration of the embedded unit cell.

Additionally, the displacement modes at key points on the dispersion curves (points C1, C2, and C3 in Fig. A2(a)) are extracted and shown in Fig. A2(b). It is evident that points C1, C2, and C3 correspond to the vertical resonance, torsional resonance, and bending resonance of the inner column, respectively. Although the soft coupling provided by the rubber facilitates the resonance of the inner column, the side rubber pad still imposes constraints on its vibration. Intuitively, reducing the height of the side rubber pad and introducing gaps between the outer and inner columns could decrease the lateral constraint stiffness on the inner column, thereby allowing greater freedom for resonance. For this reason, we optimize the rubber arrangement by shortening the side rubber pad, as depicted in Fig. A1(b). The configuration in Fig. A1(b) represents our final unit cell design shown in Fig. 1, yielding wider bandgaps, as illustrated in Fig. 3(b).

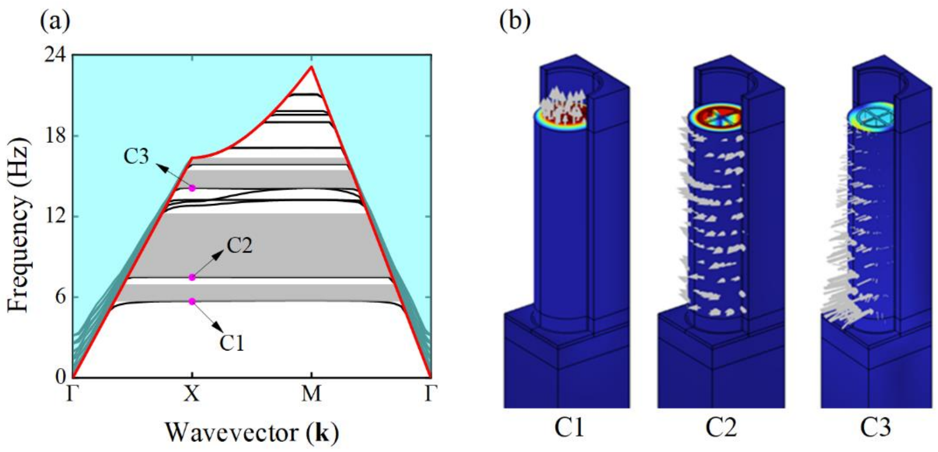

Figure A2. (a) Bandgap results of the unit cell in Fig. A1(a); (b) Mode shapes of points C1, C2, and C3 in (a).

Acknowledgement

The research is supported part by the start-up fund provided by the Hong Kong Polytechnical University, and part by the research project fund from Research Institute for Sustainable Urban Development (RISUD).

References

[1] Mu D, Shu HS, Zhao L, An SW. A Review of Research on Seismic Metamaterials. Adv Eng Mater. 2020;22.

[2] Spencer BF, Nagarajaiah S. State of the art of structural control. J Struct Eng. 2003;129:845-56.

[3] Mori A, Carr AJ, Cooke N, Moss PJ. Compression behaviour of bridge bearings used for seismic isolation. Eng Struct. 1996;18:351-62.

[4] Zhao ZP, Hu XY, Chen QJ, Wang YC, Hong N, Zhang RF. Friction pendulum-strengthened tuned liquid damper (FPTLD) for earthquake resilience of isolated structures. Int J Mech Sci. 2023;244.

[5] Liu C, Gao R, Guo B. Seismic design method analyses of an innovative steel damping bearing for

railway bridges. Eng Struct. 2018;167:518-32.

[6] Mao HM, Yan XY, Wei XY, Liu XH. Seismic analysis of a frame structure equipped with displacement-amplified torsional dampers. Structures. 2022;41:190-202.

[7] Mazloum AA, Afshar MA, Aghaeipour S. Seismic assessment of Isolator-Damper hybrid structural system based on analysis of MDOF and modal 2DOF models. Structures. 2023;58.

[8] Zheng HZ, Miao LC, Xiao P, Lei KY, Wang Q. Novel metamaterial foundation with multi low-frequency bandgaps for isolating earthquakes and train vibrations. Structures. 2024;61.

[9] Li T, Su Q, Kaewunruen S. Seismic metamaterial barriers for ground vibration mitigation in railways considering the train-track-soil dynamic interactions. Constr Build Mater. 2020;260.

[10] Maheshwari HK, Rajagopal P. Novel locally resonant and widely scalable seismic metamaterials for broadband mitigation of disturbances in the very low frequency range of 0–33 Hz. Soil Dyn Earthquake Eng. 2022;161.

[11] He C, Zhou SH, Li XX, Di HG, Zhang XH. Forest trees as a natural metamaterial for surface wave attenuation in stratified soils. Constr Build Mater. 2023;363.

[12] Achaoui Y, Ungureanu B, Enoch S, Brûlé S, Guenneau S. Seismic waves damping with arrays of inertial resonators. Extreme Mech Lett. 2016;8:30-7.

[13] Liu WL, Yoon GH, Yi B, Yang Y, Chen Y. Ultra-wide band gap metasurfaces for controlling seismic surface waves. Extreme Mech Lett. 2020;41.

[14] Wang Y, Yang F, Yang J-S, Tong L-L, Li S, Liu Q et al. Study on vibration damping performance of a petal-shaped seismic metamaterial. Structures. 2023;56.

[15] Shi DY, Chen HL, Qiu ZY, Fan HL. Blast wave attenuation of nonlinear meta-isolation system: Theoretical analysis and experimental validation. J Build Eng. 2023;80.

[16] Wang X, Wan S, Nian Y, Zhou P, Zhu Y. Periodic in-filled pipes embedded in semi-infinite space as seismic metamaterials for filtering ultra-low-frequency surface waves. Constr Build Mater. 2021;313.

[17] Fang X, Lou J, Chen YM, Wang J, Xu M, Chuang K-C. Broadband Rayleigh wave attenuation utilizing an inertant seismic metamaterial. Int J Mech Sci. 2023;247.

[18] Luo YM, Huang TT, Zhang Y, Xu HH, Xie YM, Ren X. Novel meter-scale seismic metamaterial with low-frequency wide bandgap for Lamb waves. Eng Struct. 2023;275.

[19] Qahtan A, Huang JK, Amran M, Qader DN, Fediuk R, Wael A. Seismic Composite Metamaterial: A Review. J Compos Sci. 2022;6.

[20] Luo YM, He C, Tao Z, Hao J, Xu HH, Zhang Y et al. A surface-wave seismic metamaterial filled with auxetic foam. Int J Mech Sci. 2024;262.

[21] Miniaci M, Krushynska A, Bosia F, Pugno NM. Large scale mechanical metamaterials as seismic shields. New J Phys. 2016;18.

[22] Zeng Y, Zhang S-Y, Zhou H-T, Wang Y-F, Cao L, Zhu Y et al. Broadband inverted T-shaped seismic metamaterial. Mater Des. 2021;208.

[23] Liu Z, Dong H-W, Yu G-L, Cheng L. Achieving ultra-broadband and ultra-low-frequency surface wave bandgaps in seismic metamaterials through topology optimization. Compos Struct. 2022;295.

[24] Muhammad, Lim CW, Reddy JN. Built-up structural steel sections as seismic metamaterials for surface wave attenuation with low frequency wide bandgap in layered soil medium. Eng Struct. 2019;188:440-51.

[25] Xu R, Muzamil M, Fan L, Yuan K, Yang H, Du Q. Broadband seismic metamaterial with an improved cylinder by introducing plus-shaped structure. Europhys Lett. 2021;133.

[26] Su YC, Wang SS. Gradient V-Shaped and N-Shaped Seismic Metamaterials. Materials (Basel). 2023;16.

[27] Cai CZ, Deng SP, Xiong QW, Wu DZ, Li C. Tuning Fork Seismic Metamaterial for Low-Frequency Surface Wave Attenuation with Locally Resonant Band Gaps. J Vib Eng Technol. 2023.

[28] Du Q, Zeng Y, Xu Y, Yang H, Zeng Z. H-fractal seismic metamaterial with broadband low-frequency bandgaps. J Phys D: Appl Phys. 2018;51.

[29] Zeng Y, Xu Y, Yang H, Muzamil M, Xu R, Deng K et al. A Matryoshka-like seismic metamaterial with wide band-gap characteristics. Int J Solids Struct. 2020;185-186:334-41.

[30] Fan L, Du Q, Peng P, Liu F. Minkowski-like fractal seismic metamaterial with wide low-frequency band gaps on single and layered soil. J Phys D: Appl Phys. 2022;55.

[31] Chen H-Y, Qin Z-H, Liang S-N, Li X, Yu S-Y, Chen Y-F. Gradient-index surface acoustic metamaterial for steering omnidirectional ultra-broadband seismic waves. Extreme Mech Lett. 2023;58.

[32] Chen ZY, Wang GF, Lim CW. Artificially engineered metaconcrete with wide bandgap for seismic surface wave manipulation. Eng Struct. 2023;276.

[33] Daradkeh AM, Jalali HH. Large-scale engineered meta-barriers for attenuation of seismic surface waves. Structures. 2024;64.

[34] Wu XY, Wen ZH, Jin YB, Rabczuk TM, Zhuang XY, Djafari-Rouhani B. Broadband Rayleigh wave attenuation by gradient metamaterials. Int J Mech Sci. 2021;205.

[35] Xu Y, Xu R, Peng P, Yang H, Zeng Y, Du Q. Broadband H-shaped seismic metamaterial with a rubber coating. Europhys Lett. 2019;127.

[36] Daradkeh AM, Jalali HH, Seylabi E. Mitigation of seismic waves using graded broadband

metamaterial. J Appl Phys. 2022;132.

[37] Daradkeh AM. Wide Band-Gap Metamaterials as Seismic Shields: The University of Texas at Arlington; 2023.

[38] Lou J, Fang X, Fan H, Du J. A nonlinear seismic metamaterial lying on layered soils. Eng Struct. 2022;272.

[39] Gao L, Cai C, Mak CM, He X, Zou Y, Wu D. Surface wave attenuation by periodic hollow steel trenches with Bragg band gap and local resonance band gap. Constr Build Mater. 2022;356:129289.

[40] Zeng Y, Peng P, Du Q-J, Wang Y-S, Assouar B. Subwavelength seismic metamaterial with an ultra-low frequency bandgap. J Appl Phys. 2020;128.

[41] Liu Z, Qin KQ, Yu GL. Partially Embedded Gradient Metabarrier: Broadband Shielding from Seismic Rayleigh Waves at Ultralow Frequencies. J Eng Mech. 2020;146.

[42] Yu W, Zhou L. Seismic metamaterial surface for broadband Rayleigh waves attenuation. Mater Des. 2023;225.

[43] Zhao ZG, Wu SP, Xie J, Yang C, Yang XK, Chen SC, Liu QT. Recycle of waste tire rubber powder in a novel asphalt rubber pellets for asphalt performance enhancement. Constr Build Mater. 2023;399.

[44] Chen ZP, Liang YH, Lin YZ, Cai JM. Recycling of waste tire rubber as aggregate in impact-resistant engineered cementitious composites. Constr Build Mater. 2022;359.

[45] Hu H, Papastergiou P, Angelakopoulos H, Guadagnini M, Pilakoutas K. Mechanical properties of SFRC using blended Recycled Tyre Steel Cords (RTSC) and Recycled Tyre Steel Fibres (RTSF). Constr Build Mater. 2018;187:553-64.

[46] Zhang K, Luo J, Hong F, Yu J, Zhao C, Deng Z. Graded Seismic Metamaterials with Structural Steel Sections for Low-Frequency Isolation of Surface Wave. Int J Struct Stab Dyn. 2023;23.

[47] Badreddine Assouar M, Oudich M. Dispersion curves of surface acoustic waves in a two-dimensional phononic crystal. Appl Phys Lett. 2011;99.

[48] Achaoui Y, Khelif A, Benchabane S, Robert L, Laude V. Experimental observation of locally-resonant and Bragg band gaps for surface guided waves in a phononic crystal of pillars. Physical Review B. 2011;83.

[49] Khelif A, Achaoui Y, Benchabane S, Laude V, Aoubiza B. Locally resonant surface acoustic wave band gaps in a two-dimensional phononic crystal of pillars on a surface. Physical Review B. 2010;81.

[50] Bai YT, Li XL, Liao YW. Bio-inspired branch structure seismic metamaterial: attenuating low-frequency Rayleigh waves. Journal of Physics D-Applied Physics. 2024;57.

[51] Cai RC, Jin YB, Djafari-Rouhani B, Zhou SW, Chen PX, Rabczuk T et al. Attenuation of Rayleigh and pseudo surface waves in saturated soil by seismic metamaterials. Comput Geotech. 2024;165.

[52] Muzamil M, Yang HW, Xu R, Zeng Y, Peng P, Du QJ. A petal-cylindrical seismic metamaterial occupying low-frequency wide bandgaps in horizontally stratified soils. Wave Motion. 2023;122.

[53] Shi N, Liu H, Wang L, Ji J, Li Z, Guo S, Wang J. Double-gradient seismic metamaterials with zero-frequency bandgap characteristic in a layered soil medium. Europhys Lett. 2023;144.

[54] Pu XB, Shi ZF. Broadband surface wave attenuation in periodic trench barriers. J Sound Vib. 2020;468.

[55] Yesilyurt A, Akram MR, Zulfikar AC. Assessment of engineering demand parameters through SHM for RC-structures. J Civ Struct Health Monit. 2019;9:253-61.

[56] Zlatanovic E, Lukic DC, Prolovic V, Bonic Z, Davidovic N. Comparative study on earthquake-induced soil-tunnel structure interaction effects under good and poor soil conditions. Eur J Environ Civ Eng. 2015;19:1000-14.

[57] Boatwright J. Quasi-dynamic models of simple earthquakes: Application to an aftershock of the 1975 Oroville, California, earthquake. Bull Seismol Soc Am. 1981;71:69-94.

[58] Felzer KR, Kilb D. A case study of two M ~5 mainshocks in Anza, California: Is the footprint of an aftershock sequence larger than we think? Bull Seismol Soc Am. 2009;99:2721-35.

[59] Wang W, Guan W, Dou Y, Zhou Y. Attenuation analysis of low-frequency surface waves in the ultra-low-frequency bandgap of embedded seismic metamaterials. Mech Adv Mater Struct. 2023:1-11.